

## RESEARCH ARTICLE

## SUPERCONDUCTIVITY

# Tuning superconductivity in twisted bilayer graphene

Matthew Yankowitz<sup>1\*</sup>, Shaowen Chen<sup>1,2\*</sup>, Hryhorii Polshyn<sup>3\*</sup>, Yuxuan Zhang<sup>3</sup>, K. Watanabe<sup>4</sup>, T. Taniguchi<sup>4</sup>, David Graf<sup>5</sup>, Andrea F. Young<sup>3,†</sup>, Cory R. Dean<sup>1,†</sup>

Materials with flat electronic bands often exhibit exotic quantum phenomena owing to strong correlations. An isolated low-energy flat band can be induced in bilayer graphene by simply rotating the layers by 1.1°, resulting in the appearance of gate-tunable superconducting and correlated insulating phases. In this study, we demonstrate that in addition to the twist angle, the interlayer coupling can be varied to precisely tune these phases. We induce superconductivity at a twist angle larger than 1.1°—in which correlated phases are otherwise absent—by varying the interlayer spacing with hydrostatic pressure. Our low-disorder devices reveal details about the superconducting phase diagram and its relationship to the nearby insulator. Our results demonstrate twisted bilayer graphene to be a distinctively tunable platform for exploring correlated states.

The electronic properties of many materials are well described by assuming that non-interacting electrons simply fill the available energy bands. However, for systems with narrowly dispersing flat bands in which the kinetic energy is small relative to the Coulomb energy, the assumption that electrons are noninteracting is no longer valid. Instead, the electronic ground state is driven by minimizing the mutual Coulomb repulsion between electrons. It has recently been demonstrated that heterostructures consisting of layered two-dimensional materials—in which narrow isolated bands can be realized simply by tuning the rotational ordering between layers (1–4)—provide a simple avenue to reach this condition. Bilayer graphene, which normally consists of two vertically stacked monolayer graphene layers arranged in an AB (Bernal) stacking configuration, provides a notable example. Upon rotating the layers away from Bernal stacking to the so-called “magic angle” of ~1.1°, the interplay between the resulting moiré superlattice and hybridization between the layers leads to the formation of an isolated flat band at the charge neutrality point (CNP) (1). Near this flat-band angle, recent experiments have demonstrated correlated insulator phases at half-band filling (5) and superconductivity upon doping slightly away from half-band filling for hole-type carriers (6).

The discovery of superconductivity in twisted bilayer graphene (tBLG) has sparked intense interest, owing in part to the possibility that it arises from an unconventional electron-mediated pairing mechanism. The material composition is very simple, comprising only carbon atoms. Unlike most unconventional superconductors, for which exploring different carrier density requires growing different samples, in tBLG the entire correlated phase diagram can be accessed in a single device by field-effect gating. Additionally, the available degrees of freedom in tBLG, including twist angle control (1), interlayer separation (7, 8), and displacement field-induced layer imbalance (1, 9), provide opportunities to experimentally tune the electronic structure in ways that have proven difficult or impossible in previously investigated superconductors.

Here we present measurements of both the superconducting and correlated insulating states in tBLG at the flat-band condition. We study three separate devices, fabricated in a fully encapsulated, dual-graphite gate structure to enhance device mobility and minimize effects of charge inhomogeneity (10). Two devices have twist angles close to 1.1° and exhibit superconductivity and correlated insulating phases. The third device is fabricated at a twist angle of 1.27°, and although correlated phases are absent, we demonstrate the ability to induce them by applying hydrostatic pressure (11).

## Correlated phases in tBLG

We fabricate boron nitride (BN)-encapsulated tBLG using the “tear-and-stack” method to control the graphene alignment (12) and additionally include top and bottom graphite gates (Fig. 1A). The all-van der Waals device geometry has previously been shown to substantially increase charge homogeneity as compared with the evaporated metal or degenerately doped silicon gates

(10). Additionally, the dual-gate structure allows us to independently vary the charge carrier density and transverse displacement field and experimentally investigate the effects of interlayer bias on the correlated states (1, 9, 13).

Figure 1B shows the density-dependent resistance of device D1, with interlayer twist angle  $\theta \approx 1.14^\circ$ . The device exhibits low charge carrier inhomogeneity of  $\delta n < 2 \times 10^{10} \text{ cm}^{-2}$ , as measured by the full width at half maximum of the resistance peak at the CNP. The low charge disorder is further confirmed by the emergence of fractional quantum Hall states at magnetic fields as low as ~4 T (14). In Fig. 1B, the resistance is plotted over nearly the full density range of the flat band. We identify the boundaries of the flat band by the appearance of strongly insulating response at densities symmetrically located around the CNP (14). We then use a normalized density scale to define partial band filling, with  $+n_s$  and  $-n_s$  corresponding to the electron- and hole-doped band edges with  $\pm 4$  electrons per moiré unit cell, respectively. Within the flat band, we observe resistive states at the CNP, as well as at  $\pm n_s/2$  and  $+3n_s/4$ . At a base temperature of ~10 mK, regions of superconductivity appear both in the hole- and electron-doped regions, with the resistance dropping to zero for densities near  $\pm n_s/2$ .

In the hole band, the density and magnetic field dependence of the superconducting response resembles that observed previously (6), whereas the electron-band superconductivity was not previously reported. In both bands, superconductivity appears more robust on the high-density side of the insulator,  $|n| > |\pm n_s/2|$ , and is much weaker or absent on the low-density side,  $|n| < |\pm n_s/2|$ . In the hole band, the low-density pocket is not fully superconducting at 10 mK, whereas in the similar doping range for the electron band, no signature of superconductivity appears down to base temperature.

Figure 1C shows the resistance versus temperature measured at optimal doping of both the hole- and electron-type superconducting pockets. The critical temperature ( $T_c$ )—defined as the crossover point of linear fits to the low- and high-temperature portions of the resistance curves on a logarithmic scale—is ~0.25 K for electron-type carriers and ~0.4 K for hole-type carriers. The hole-band  $T_c$  is similar to that reported previously for a similar twist angle (6); however, superconductivity for electron-type carriers in tBLG was not observed in that work. Although the band structure of tBLG is not anticipated to be precisely particle-hole symmetric, the observation of superconductivity over similar ranges of density for both electron and hole carriers suggests a connection between the mechanisms driving the superconducting phases of the two carrier types.

## Influence of structural inhomogeneity

Despite the reduction of charge disorder effects in our dual-graphite gated structure, we observe strong signatures of inhomogeneity in the transport response. Most obviously, the carrier density corresponding to full filling is observed to vary

<sup>1</sup>Department of Physics, Columbia University, New York, NY 10027, USA. <sup>2</sup>Department of Applied Physics and Applied Mathematics, Columbia University, New York, NY 10027, USA. <sup>3</sup>Department of Physics, University of California, Santa Barbara, CA 93106, USA. <sup>4</sup>National Institute for Materials Science, 1-1 Namiki, Tsukuba 305-0044, Japan. <sup>5</sup>National High Magnetic Field Laboratory, Tallahassee, FL 32310, USA.

\*These authors contributed equally to this work.

†Corresponding author. Email: afy2003@ucsb.edu (A.F.Y.); cd2478@columbia.edu (C.R.D.)

between different pairs of contacts (fig. S1F) (14). This suggests that the moiré unit cell area is not uniform over the whole device, and we have observed variations of the moiré unit cell area by as much as  $\sim 30\%$  within a single device (14). This is consistent with recent transmission electron microscopy imaging of tBLG devices with similar twist angles (15), suggesting spatial variations in the moiré period may be ubiquitous in these structures.

Additionally, we can use our dual-gated structure to investigate the device response with applied displacement field (Fig. 1D). The transport properties of graphene bilayers are typically strongly dependent on displacement field ( $D$ ) (16); however, theoretical modeling of flat-band tBLG suggests that transverse field should have little to no consequence because of the strong interlayer hybridization (1, 9, 13). The superconducting regions in our device appear to be largely insensitive to  $D$ , exhibiting, for instance, similar  $T_c$  at large positive and large negative values of  $D$  (fig. S9) (14). In contrast, the insulating state at  $-n_s/2$  shows a strong dependence on  $D$ , with resistance exceeding 10 kilohms for positive  $D$  but appearing to drop to zero for negative  $D$ . Similarly, the peak resistance at  $+3n_s/4$  in the electron band also varies strongly but exhibits the opposite dependence, becoming

less resistive at large, positive  $D$ . This opposite trend with  $D$  between the electron and hole bands suggests that the insulating state is suppressed when the carriers of either sign are polarized toward the same (top) graphene layer. Because freestanding tBLG is expected to be symmetric under layer interchange, this response is unexpected and likely to be extrinsic.

We conjecture that the superconductor-to-insulator transition observed at  $-n_s/2$  is another consequence of structural inhomogeneity. In particular, polarizing carriers to a more strained graphene layer may favor formation of a percolating superconducting network that short-circuits the insulating phase at  $-n_s/2$ . Although this may also arise as a consequence of charge disorder, the measured charge inhomogeneity is  $\sim 10^{10} \text{ cm}^{-2}$ , insufficient to mix these phases across their native separation in carrier density, which is an order of magnitude larger.

Finally, evidence of a percolating superconducting network is provided by measurements of the differential resistance  $dV/dI$  as a function of applied current  $I_{dc}$  and magnetic field  $B$ . Figure 1, E to G, shows three different measurements, sampling different regions of the  $D$ -versus- $n$  response shown in Fig. 1D. Periodic oscillations in the critical current  $I_c$ , resembling Fraunhofer

interference, suggest quantum phase coherent transport arising from interspersed regions of superconducting and metallic or insulating phases within the device. The period of the oscillations  $\Delta B$  varies from 2 to 4 mT, indicating an effective junction area of  $S \approx 0.5$  to  $1 \mu\text{m}^2$ , using  $S = \Phi_0/\Delta B$ , where  $\Phi_0 = h/2e$  is the superconducting flux quantum,  $h$  is Planck's constant, and  $e$  is the charge of the electron. This constitutes as much as  $\sim 40\%$  of the device area. Notably, Fig. 1G, measured at  $-n_s/2$  and negative  $D$ , shows a minimum in  $I_c$  at  $B = 0$ , with  $I_c$  increasing to a maximum near  $\pm 4$  mT, indicative of an additional  $\pi$  phase emerging between the junctions of the device (14). The variations among the quantum interference patterns appearing in Fig. 1, E to G, confirm that the microscopic structure of superconducting regions is tunable with  $n$  and  $D$ . The prevalence of disorder-induced experimental features we identify in our device suggests that the correlated physics of tBLG is extremely sensitive to the structural details of the moiré pattern.

### Bandwidth tuning with pressure

The width of the flat bands in tBLG is determined by an interplay between the momentum-space mismatch of the Dirac cones between the

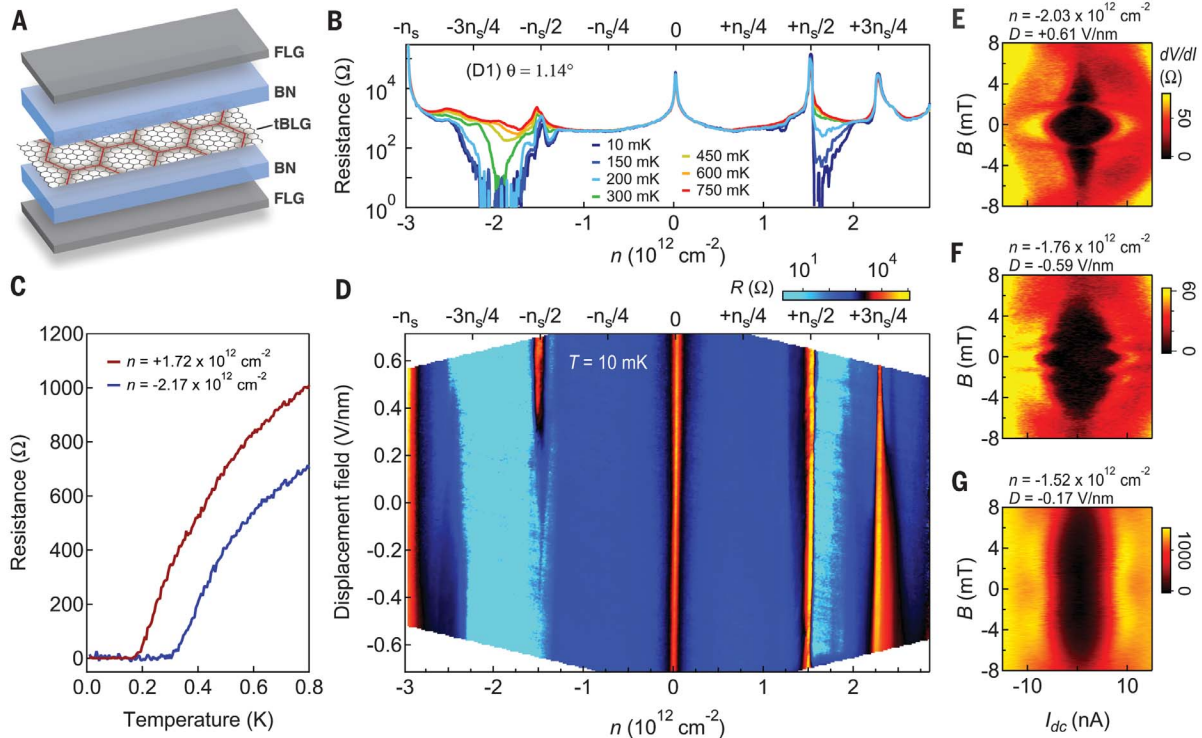


**Fig. 1. Superconductivity in a 1.14° device.** (A) Schematic of an all-van der Waals tBLG heterostructure. tBLG is encapsulated between flakes of BN, with encapsulating flakes of few-layer graphite (FLG) acting as gates. (B) Temperature dependence of the resistance of device D1 over the density range necessary to fill the moiré unit cell,  $n \in [-n_s, n_s]$  at  $D = 0$ . The resistance drops to zero over a finite range of  $n$  for electron ( $n > n_s/2$ ) and hole ( $n < -n_s/2$ ) doping. (C) Resistance as a function of temperature at optimal doping of the hole- and electron-doped superconductors in blue and red, respectively. (D) Resistance ( $R$ ) of device

D1 as a function of displacement field. At  $-n_s/2$ , an insulating phase develops at positive  $D$ , whereas a superconducting phase develops at negative  $D$ . (E to G) Fraunhofer-like quantum interferences of the critical current, arising from one or more Josephson weak links within the sample, measured at (E)  $n = -2.03 \times 10^{12} \text{ cm}^{-2}$  and  $D = +0.61 \text{ V/nm}$ , (F)  $n = -1.76 \times 10^{12} \text{ cm}^{-2}$  and  $D = -0.59 \text{ V/nm}$ , and (G)  $n = -1.52 \times 10^{12} \text{ cm}^{-2}$  and  $D = -0.17 \text{ V/nm}$ . An anomalous quantum interference pattern with a minimum in  $I_c$  at zero field is observed in (G). The measured temperature is  $T \approx 10 \text{ mK}$  for all datasets unless otherwise noted.

graphene layers (set by the twist angle) and the strength of the layer hybridization (set by the interlayer spacing) ( $I$ ). The graphene interlayer spacing can be decreased by applying hydrostatic pressure ( $II$ ) while leaving the interlayer rotation fixed ( $14$ ). Pressure can therefore theoretically be used to achieve the flat-band condition at arbitrary twist angle, relaxing the need for precise angle tuning ( $7, 8$ ) and potentially reducing the impact of structural inhomogeneity of the moiré pattern. Furthermore, inducing the flat band at higher twist angle has been proposed as a route toward increasing the energy scale of the superconductor ( $6-8$ ).

Figure 2A shows the conductance  $G$  versus density for a device, D2, with twist angle  $\theta \approx 1.27^\circ$ . The gray curve in Fig. 2A shows the ambient pressure response. Strongly insulating states appear at full filling of the moiré unit cell  $\pm n_s$ , indicating the presence of an isolated low-energy band. However, only very weakly insulating states (conductance minima) are observed at  $\pm n_s/2$  and around  $\pm 3n_s/4$ , and no evidence of superconductivity is present, suggesting that, at this angle, the low-energy band does not support strong correlations. The blue curve shows the conductance of the same device under 2.21 GPa of hydrostatic pressure. Insulating states at several rational fillings of the moiré unit cell become evident—most notably at  $\pm n_s/2$  and  $+3n_s/4$ , as well as more weakly at  $+n_s/4$ . Figure 2B plots the conductance of the device at  $-n_s/2$  as a function of temperature for three values of pressure, illustrating the crossover from metallic to insulating behavior under pressure and consistent with pressure-induced bandwidth tuning.

In addition to strong insulating phases, we also observe a pressure-induced emergence of superconductivity. For hole doping slightly beyond  $-n_s/2$  (see caption to Fig. 2C), the device exhibits metallic temperature dependence under ambient pressure but superconducting behavior at high pressure, with the resistance rapidly dropping to the experimental noise floor of  $\sim 10$  ohms (Fig. 2C). In the pressure range that we study, the insulating gaps (measured by thermal activation; Fig. 2D) and  $T_c$  of the superconductor (Fig. 2E) vary nonmonotonically with pressure, with both reaching their highest measured values at 1.33 GPa. We also observe the onset of electron-type superconductivity for electron doping just larger than  $+n_s/2$ , as evidenced by a sharp drop in the device magnetoresistance around  $B = 0$  (fig. S4B) ( $14$ ). However, it appears to have a much lower  $T_c$  than its hole-doping counterpart, preventing detailed study in pressure experiments in which our base temperature was limited to 300 mK.

Recent band structure calculations indicate that the relation between bandwidth and pressure depends on the twist angle ( $7, 8$ ). For a  $1.27^\circ$  tBLG, the minimum bandwidth is theoretically predicted to be in the range of 1.3 to 1.5 GPa ( $7, 8$ ), in good agreement with the pressure value at which we observed maximum  $T_c$ . The largest measured  $T_c$  we induce with pressure is  $\sim 3$  K, nearly an order of magnitude larger than observed in device D1 and roughly a factor of

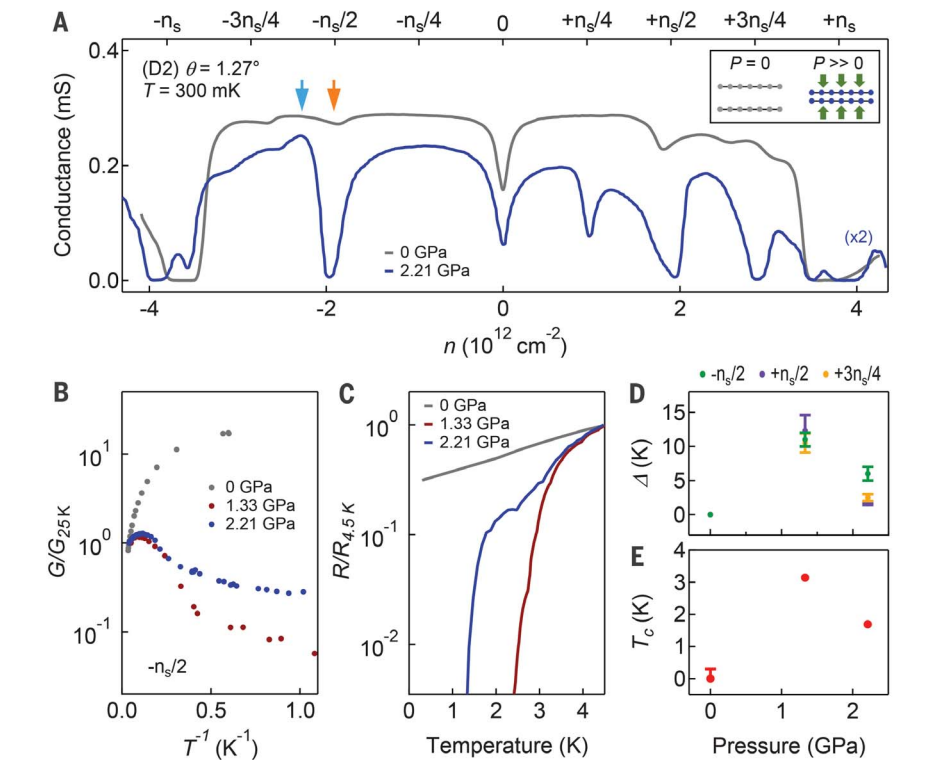


**Fig. 2. Driving superconductivity and correlated insulating states with pressure.** (A) Conductance of device D2 ( $1.27^\circ$ ) measured over the entire density range necessary to fill the moiré unit cell at two values of pressure: 0 GPa (gray) and 2.21 GPa (blue) at  $T = 300$  mK. Correlated insulating phases are only very weakly resistive at 0 GPa but develop into strongly insulating states at high pressure. The conductance is measured in a two-terminal voltage bias configuration and includes the contact resistance. (Inset) Schematic illustrating the decrease in interlayer spacing of the tBLG under high pressure ( $P$ ). (B) Device conductance versus  $T^{-1}$  at  $-n_s/2$ , normalized to its value at  $T = 25$  K [acquired at the density marked by the orange arrow in (A)]. (C) Four-terminal device resistance versus  $T$  for hole doping slightly larger than  $-n_s/2$ , normalized to its value at  $T = 4.5$  K. The device is a metal at 0 GPa but becomes a superconductor at high pressure. The two curves at high pressure are taken at optimal doping of the superconductor, and the curve at 0 GPa is taken at the same density as the 1.33-GPa curve [acquired roughly at the density marked by the blue arrow in (A)]. (D) Energy gaps  $\Delta$  of the correlated insulating phases versus pressure, extracted from the thermal activation measurements in (B) and fit according to  $G(T) \propto e^{-\Delta/kT}$ , where  $k$  is the Boltzmann constant. Error bars in the gaps represent the uncertainty arising from determining the linear (thermally activated) regime for the fit. (E)  $T_c$  of the superconducting phase versus pressure.  $T_c$  is defined as the crossover point between low- and high-temperature linear fits to the curves in (C). The upper bound for the 0-GPa curve represents the base temperature of the refrigerator.

2 larger than reported by Cao *et al.* ( $6$ ). This relative increase in  $T_c$  could be generated by an increase in the Coulomb interaction energy scale, resulting from the reduced moiré wavelength at the larger twist angle of this device ( $6-8$ ), but it may also relate to differences in sample disorder.

The device resistance around  $-n_s/2$  as a function of temperature  $T$  and magnetic field  $B$  is plotted in Fig. 3, A and B, respectively, under a pressure of 1.33 GPa. We observe a state with strongly insulating temperature dependence at  $-n_s/2$ , with a pocket of superconductivity at slightly larger hole doping and metallic behavior at slightly smaller hole doping. Our results differ from those for our device D1 and for the devices reported in ( $6$ ) in several ways. First, the device resistance in Fig. 3A grows quickly

as the temperature is lowered, whereas in prior devices it drops toward zero (e.g., negative values of  $D$  for device D1). Second, we observe a pocket of superconductivity only for  $n < -n_s/2$ , whereas prior devices additionally exhibit superconductivity for  $n > -n_s/2$ . Third, we find evidence for a metallic phase separating the superconducting and insulating phases. Although this is partially obscured in Fig. 3A by an anomalous region of apparent negative resistance arising from a measurement artifact (colored in white), measurements using other contacts (as well as similar measurements at 2.21 GPa) exhibit clearer evidence of the metallic phase (figs. S2 and S3) ( $14$ ). However, small remnant disorder may also be responsible for this apparent metallic phase, and further investigation is necessary to probe the

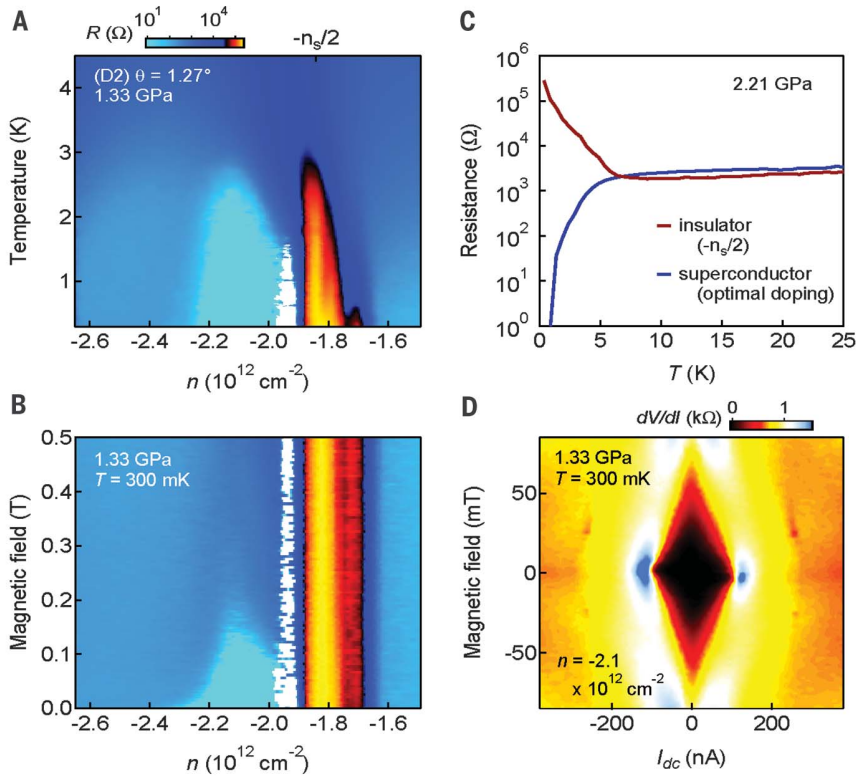


**Fig. 3. Phase diagram of tBLG under pressure.** (A) Resistance of device D2 ( $1.27^\circ$ ) over a small range of carrier density near  $-n_s/2$  versus  $T$ . An insulating phase at  $-n_s/2$  neighbors a superconducting pocket at slightly larger hole doping. An apparent metallic phase separates the two (14) but is obscured by a region of artificially negative resistance in the contacts used for this measurement (colored in white). (B) Similar map as a function of  $B$ . (C) Resistance as a function of  $T$  at 2.21 GPa at  $-n_s/2$  (red) and at optimal doping of the superconductor (blue). (D) Map of  $dV/dI$  versus  $I_{dc}$  and  $B$  at  $n = -2.1 \times 10^{12} \text{ cm}^{-2}$ ,  $T = 300 \text{ mK}$ , and 1.33 GPa. The map was acquired by using different contacts from (A) and (B) and, in particular, exhibits a lower upper critical field  $H_{c2}$ .

potential existence of a quantum critical point around this doping.

Figure 3C shows a comparison of resistance versus temperature of the insulating (red) and superconducting (blue) states, measured at 2.21 GPa. Notably, the two phases onset at similar temperatures, with the resistance in both cases diverging at  $\sim 5 \text{ K}$  from the high-temperature metallic behavior. Similar behavior is also observed in device D1, where additionally we found that similar critical currents quench each phase to the normal state resistance (fig. S8) (14). These observations suggest that the insulating and superconducting phases share similar energy scales, constraining models in which the superconductivity arises as a daughter-state of the insulator.

The lack of strong magnetoresistance oscillations in Fig. 3B suggests that sample D2 is highly homogeneous. To confirm this, we plot  $dV/dI$  as a function of  $B$  and  $I_{dc}$  in Fig. 3D and find that  $I_c$  decreases roughly linearly with  $B$  and, unlike device D1, does not exhibit quantum interference patterns associated with junction-limited superconductivity. We have additionally measured the phase diagram of this device as a function of  $D$  and do not observe a substantial displacement field dependence (in particular, there is a robust

insulating state at  $-n_s/2$  for all  $D$ ) (fig. S4A) (14). We interpret these observations to indicate that this device is less disordered than those previously reported, suggesting that details of the associated superconducting and insulating response may more faithfully represent the disorder-free phase diagram. The reasons for the reduced disorder in this sample are not fully understood. This may be emblematic of devices with larger twist angles, for which the combination of smaller moiré period and applied pressure minimizes the contribution of spatial inhomogeneity. However, owing to the limited sample size, we also cannot rule out random sample-to-sample variation. A systematic study of the interplay between twist angle and pressure—preferably in a single device (11, 17)—will be needed to resolve these issues.

### Quantum oscillations and new Fermi surfaces

The high degree of structural and charge homogeneity in our samples further allows high-resolution measurements of magnetoresistance oscillations associated with cyclotron motion of electrons. Quantum oscillations at low magnetic fields provide detailed information about electronic band structure, as their periodicity can be

used to infer the areal size of the Fermi surface. Moreover, their degeneracy reflects the presence of spin, valley, and layer degrees of freedom. Figure 4A shows magnetoresistance data from device D2 at 1.33 GPa. Several sets of seemingly independent Landau fans are observed, indicated schematically in Fig. 4B. In contrast to devices with larger twist angles, none of the quantum oscillations show  $D$ -tuned Landau level crossings (fig. S4, C and D) (14). Near the CNP, we observe a fourfold degenerate sequence of quantum oscillations, with dominant minima at  $\nu = \pm 4, \pm 8, \pm 12, \dots$  at low magnetic field, where  $\nu = nh/(eB)$  is the Landau level filling factor relative to charge neutrality.

At  $+n_s/4, \pm n_s/2$ , and  $\pm 3n_s/4$ , the carrier density extracted from the Hall effect approaches zero (fig. S5) (14), indicating the formation of new, small Fermi surfaces. These fillings also spawn independent series of quantum oscillations. At  $\pm n_s/2$ , oscillations clearly exhibit twofold degeneracy at very low fields, suggesting that the combined spin and valley degeneracy is partially lifted (6). In contrast, the sequences of quantum oscillations emerging from  $\pm 3n_s/4$  exhibit no additional degeneracy, suggesting that all degeneracies are lifted in these Fermi surfaces. Notably, the associated quantum oscillations disperse only in a single direction for each carrier type (away from the CNP) and abruptly terminate at the next commensurate filling, consistent with strong, asymmetric renormalization of the effective mass across the gap.

The sequence emerging from  $+n_s/4$  appears to be twofold degenerate but, interestingly, is odd-dominant, with primary oscillations observed at  $\nu = +1, +3, +5, \dots$ , where  $\nu$  is defined relative to  $+n_s/4$ . Although neither a resistive state nor quantum oscillations are observed originating from  $-n_s/4$ , we observe a shift in the dominant filling sequence for the CNP fan when the carrier density reaches  $-n_s/4$ . Around this density, the most-pronounced oscillations transition from a  $\nu = -4, -8, -12, \dots$  sequence near the CNP to  $\nu = -10, -14, -18, \dots$  for  $n < -n_s/4$ . Figure 4, C and D, shows a detailed view of this transition, highlighting the crossover of the dominant sequence. Notably, a qualitatively identical sequence of quantum oscillations was observed in another device at ambient pressure but with twist angle  $\theta = 1.08^\circ$ , close to the native flat-band angle (fig. S6A) [see (14) for details of this device, labeled D5]. The concordance between quantum oscillation patterns—a detailed probe of the Fermi surface—for both angle- and pressure-tuned flat-band devices supports the hypothesis that interlayer coupling and twist angle are equivalent electron structure control parameters (1, 7, 8).

The agreement between the fine structure of the quantum oscillations across devices suggests that they are a universal feature of the tBLG electronic structure near the flat-band condition; however, several features of the observed patterns are not captured by available theoretical models. Available models predict eightfold degeneracy near the CNP, arising from spin, valley, and layer degrees of freedom (18); however, we observe only

a fourfold quasi-degeneracy. Our observed filling sequence (defined as the sequence of best-resolved quantum oscillations) is identical to that in Bernal-stacked bilayer graphene, where interlayer tunneling leads to band hybridization and parabolically dispersing low-energy bands. Quadratic band touching reminiscent of Bernal bilayer graphene does feature in several recent models of tBLG flat bands (19, 20), although these models also feature additional Dirac crossings at low energy whose effect on the quantum oscillations has not been discussed in detail.

The phase shifts of the dominant oscillations observed near  $\pm n_s/4$  are also not anticipated theoretically. Quantum oscillation measurements in a tilted magnetic field (figs. S6, C and D) (14) for the Landau fan originating at the CNP reveal that the dominant symmetry-breaking term splits the valleys, rather than the spins, implying that the phase shift observed near  $-n_s/4$  arises from a crossing between spin-degenerate Landau level doublets. This implies that within a nominally spin- and valley-degenerate Landau level, the valley degeneracy is lifted most strongly at the single-particle level. Assuming valley to be a good quantum number, a magnetic field-induced valley splitting precludes perfect inversion symmetry. In contrast, most band-

structure models of this system feature inversion symmetry.

### Isospin ordering of the correlated insulators

Our observation that superconductivity appears only at densities coincident with lower-degeneracy quantum oscillations near half-filling—but not near insulating states at quarter- and three-quarter filling—suggests that the nature of symmetry breaking may be integral to superconductivity. A wide array of candidate states have already been proposed in the literature to describe the correlated insulating states, including antiferromagnetic Mott insulators, charge density waves, Wigner crystals, and isospin ferromagnetic band insulators (18, 21–27). Parallel magnetic field measurements offer a simple probe of isospin physics, as a primary effect of  $B_{\parallel}$  is to increase the Zeeman energy. Under applied  $B_{\parallel}$ , the gap of a spin-unpolarized (valley-polarized) ground state should decrease linearly, whereas the gap is expected to increase linearly, or remain unchanged, for spin-polarized (valley-unpolarized) ground-state ordering.

Figure 5A shows the parallel magnetic-field response of the conductance of device D3, with twist angle  $\theta \approx 1.10^\circ$ . The conductance at zero magnetic field exhibits minima at the CNP,  $\pm n_s/$

2, and  $+3n_s/4$  band filling, along with more weakly developed features at  $-3n_s/4$  and  $+n_s/4$ . At  $\pm n_s/2$  filling, the conductance minimum fades with increasing  $B_{\parallel}$ , whereas the opposite behavior is observed at  $\pm n_s/4$ . The  $\pm 3n_s/4$  states are insensitive to magnetic field (fig. S11B) (14). Qualitatively, our observations suggest that the  $\pm n_s/2$  insulators are spin-unpolarized, whereas both the  $\pm n_s/4$  and  $\pm 3n_s/4$  are spin-polarized.

We explore this picture quantitatively using the thermal activation gap of the  $\pm n_s/2$  state—the only commensurate insulator that shows clear thermal activation in this device—as a function of  $B_{\parallel}$  (Fig. 5B). Unexpectedly, it closes nonlinearly with  $B_{\parallel}$ , inconsistent with either full spin or valley polarization. The approximately parabolic decrease is also not consistent with antiferromagnetically aligned spins in opposite valleys, which would lead to an increasing gap at larger  $B_{\parallel}$ . Our finding suggests that isospin ordering alone, without additional symmetry breaking that lifts the degeneracy of the Dirac band touching, may be insufficient to explain the nature of the half-filling insulators.

### Discussion

Accurate modeling of tBLG is complicated by the large size of the moiré unit cell, which prevents

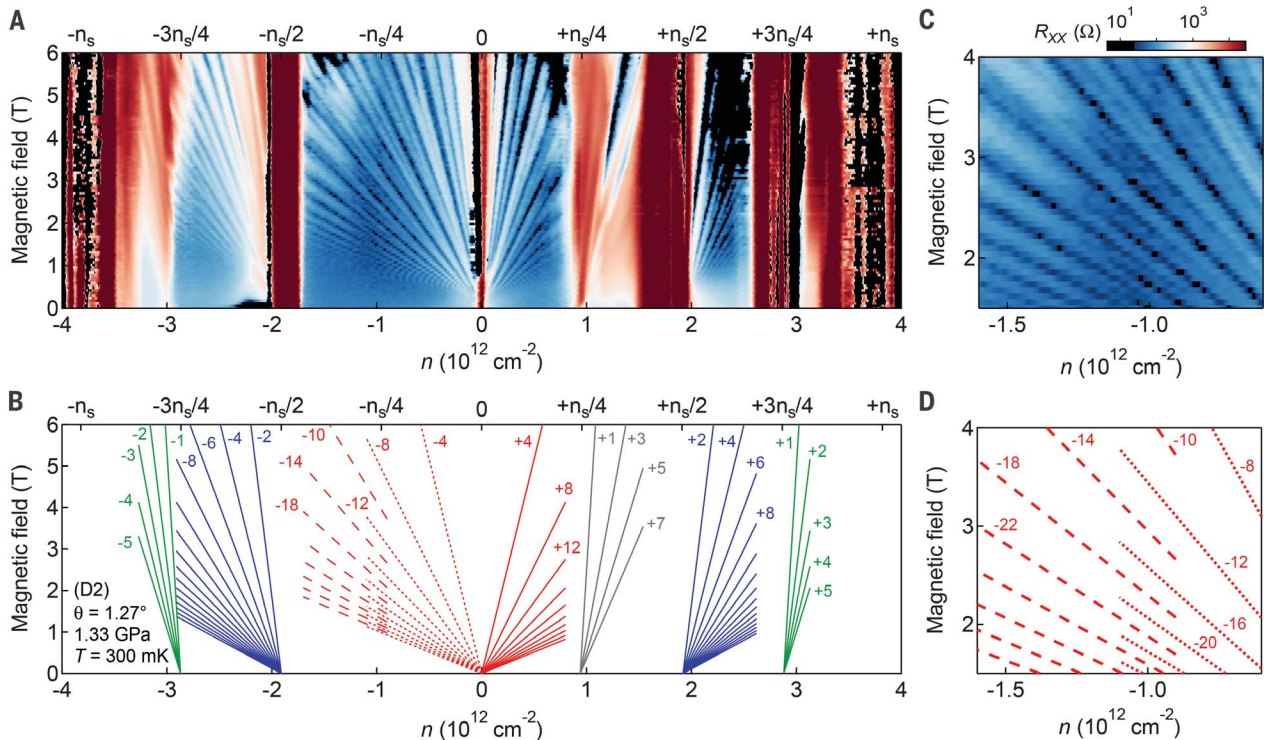


**Fig. 4. Quantum oscillations in flat-band tBLG.** (A) Landau fan diagram of device D2 ( $1.27^\circ$ ) at 1.33 GPa up to full filling of the moiré unit cell at  $T = 300$  mK. Quantum oscillations emerge from the CNP with a dominant degeneracy sequence of  $\nu = \pm 4, \pm 8, \pm 12, \dots$  at low field. Separate sequences of quantum oscillations emerge from  $\pm n_s/4$  with a dominant sequence of  $\nu = +1, +3, +5, \dots$  from  $\pm n_s/2$  with a dominant sequence of  $\nu = \pm 2, \pm 4, \pm 6, \dots$  and from  $\pm 3n_s/4$  with a dominant sequence of  $\nu = \pm 1, \pm 2, \pm 3, \dots$ . Regions of negative measured voltage are set to zero resistance for clarity.

most prominently affecting the high-field region of the map between  $+n_s/2$  and  $+3n_s/4$ . (B) Schematic Landau level structure corresponding to the observations in (A). Only the Landau levels persisting to the lowest fields are plotted; by 6 T, states at all filling factors are observed. (C) Zoom-in view of (A) around  $-n_s/4$ . (D) Schematic Landau level structure corresponding to the observations in (C). The dominant degeneracy sequence evolves smoothly from  $\nu = -4, -8, -12, \dots$  at low density to  $\nu = -10, -14, -18, \dots$  at high density, switching around  $-n_s/4$ .

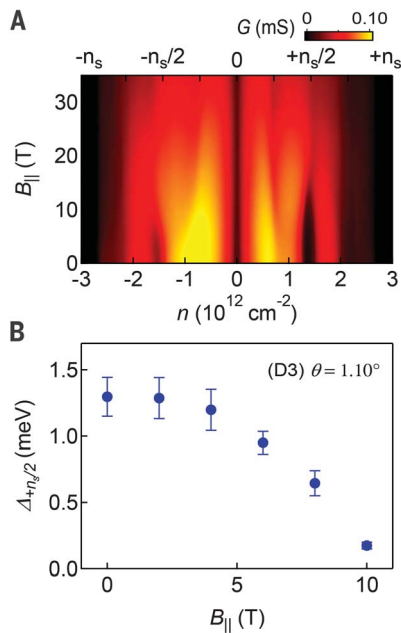


**Fig. 5. Parallel field dependence of correlated insulating states.** (A) Conductance of device D3 ( $1.10^\circ$ ) as a function of carrier density and  $B_{\parallel}$  at  $T = 300$  mK. Correlated insulating states at  $\pm n_g/2$  are less insulating at large  $B_{\parallel}$ , whereas states at  $\pm n_g/4$  are more insulating. The conductance of states at  $\pm 3n_g/4$  and at the CNP is roughly independent of  $B_{\parallel}$ . (B) Energy gap of the correlated insulating state at  $+n_g/2$  at various  $B_{\parallel}$  measured by thermal activation (fig. S11A). Error bars in the gaps represent the uncertainty arising from determining the linear (thermally activated) regime for the fit.

reliable band structure calculations. Moreover, emerging literature suggests a wide variety of plausible mechanisms and ground states for both the superconducting and insulating states. Many of these models predict unconventional all-electronic pairing mechanisms (21, 23–25, 28–34, 35–39), whereas others are either explicitly or implicitly consistent with conventional phonon-mediated superconductivity (27, 40–44). Our data, taken together, highlight a number of constraints any successful theory of tBLG should satisfy, which we summarize here.

First, our experiments confirm the basic notion that correlation physics in tBLG arises from the interplay of angular misalignment and interlayer tunneling ( $I$ ). We observe insulating and superconducting states in the same regime of angles as in (5, 6) at ambient pressure, and our finite-pressure experiments show the anticipated trend, with flat-band physics appearing at larger angles for larger applied pressure. The small and likely extrinsic effect of displacement field is similarly consistent with expectations of strong interlayer hybridization.

However, our data reveal several important new details of the resulting correlated states themselves. Most importantly, our data suggest

that the intrinsic domain of superconductivity in this system is restricted to a narrow range of charge density at higher absolute density—but not lower—than half-filling (i.e.,  $|n| > |\pm n_g/2|$ ). Superconductivity occurs for both electron and hole doping and is nearly adjacent to a strongly insulating state. The domain of superconductivity coincides with that of twofold degenerate quantum oscillations, indicating that a small Fermi surface with reduced degeneracy is nucleated at  $n_g/2$ . Although we cannot exclude superconducting states with transitions at temperatures lower than our experimental base temperature, we fail to observe superconductivity near other commensurate fillings, including several that host similar insulating states. This suggests that the nature of the Fermi surface nucleated  $\pm n_g/2$  may be essential to the onset of nearby superconductivity, although whether this is via a purely electronic mechanism, an enhancement of density of states that favor a phonon-mediated mechanism, or some mechanism yet to be proposed is unknown.

Finally, our results suggest that future work should focus on improving the spatial homogeneity of the tBLG moiré pattern. In this study, we realized a small electronic bandwidth in a device with a smaller moiré period by applying pressure. Local strains in the graphene lattice result in smaller fluctuations of the moiré period as the overall moiré period is reduced (15); therefore, we anticipate that applying higher pressure to a device with even larger twist angle could result in further improvements to the device homogeneity. Additionally, the smaller moiré period is anticipated to drive stronger Coulomb repulsion, potentially leading to larger energy scales for the superconducting and correlated insulating phases (6–8). Reliable fabrication of highly homogeneous samples will be critical for further progress in elucidating the mechanisms driving the correlated phases observed in these systems, especially in experiments performed without the use of pressure.

## REFERENCES AND NOTES

- B. Bistritzer, A. H. MacDonald, *Proc. Natl. Acad. Sci. U.S.A.* **108**, 12233–12237 (2011).
- G. Chen et al., *Nat. Phys.* **10**, 1038/s41567-018-0387-2 (2019).
- F. Wu, T. Lovorn, E. Tutuc, A. H. MacDonald, *Phys. Rev. Lett.* **121**, 026402 (2018).
- Y.-H. Zhang, D. Mao, Y. Cao, P. Jarillo-Herrero, T. Senthil, *Phys. Rev. B* **99**, 075127 (2019).
- Y. Cao et al., *Nature* **556**, 80–84 (2018).
- Y. Cao et al., *Nature* **556**, 43–50 (2018).
- S. Carr, S. Fang, P. Jarillo-Herrero, E. Kaxiras, *Phys. Rev. B* **98**, 085144 (2018).
- B. L. Chittari, N. Leconte, S. Javvaji, J. Jung, *Electron. Struct.* **1**, 015001 (2019).
- G. Trambly De Laissardière, O. F. Namarvar, D. Mayou, L. Magaud, *Phys. Rev. B* **93**, 235135 (2016).
- A. A. Zibrov et al., *Nature* **549**, 360–364 (2017).
- M. Yankowitz et al., *Nature* **557**, 404–408 (2018).
- K. Kim et al., *Nano Lett.* **16**, 1989–1995 (2016).
- K. Kim et al., *Proc. Natl. Acad. Sci. U.S.A.* **114**, 3364–3369 (2017).
- See supplementary materials.
- H. Yoo et al., arXiv:1804.03806 [cond-mat.mtrl-sci] (11 April 2018).
- Y. Zhang et al., *Nature* **459**, 820–823 (2009).
- R. Ribeiro-Palau et al., *Science* **361**, 690–693 (2018).
- N. F. Q. Yuan, L. Fu, *Phys. Rev. B* **98**, 045103 (2018).

- Z. Song et al., arXiv:1807.10676 [cond-mat.mes-hall] (27 July 2018).
- K. Hejazi, C. Liu, H. Shapourian, X. Chen, L. Balents, *Phys. Rev. B* **99**, 035111 (2019).
- C. Xu, L. Balents, *Phys. Rev. Lett.* **121**, 087001 (2018).
- H. C. Po, L. Zou, A. Vishwanath, T. Senthil, *Phys. Rev. X* **8**, 031089 (2018).
- B. Roy, V. Juricic, arXiv:1803.11190 [cond-mat.mes-hall] (29 March 2018).
- G. Baskaran, arXiv:1804.00627 [cond-mat.supr-con] (2 April 2018).
- H. Isobe, N. F. Q. Yuan, L. Fu, *Phys. Rev. X* **8**, 041041 (2018).
- B. Padhi, C. Setty, P. W. Phillips, *Nano Lett.* **18**, 6175–6180 (2018).
- M. Ochi, M. Koshino, K. Kuroki, *Phys. Rev. B* **98**, 081102(R) (2018).
- H. Guo, X. Zhu, S. Feng, R. T. Scalettar, *Phys. Rev. B* **97**, 235453 (2018).
- T. Huang, L. Zhang, T. Ma, arXiv:1804.06096 [cond-mat.supr-con] (17 April 2018).
- L. Zhang, arXiv:1804.09047 [cond-mat.mes-hall] (24 April 2018).
- S. Ray, T. Das, arXiv:1804.09674 [cond-mat.supr-con] (25 April 2018).
- C.-C. Liu, L.-D. Zhang, W.-Q. Chen, F. Yang, *Phys. Rev. Lett.* **121**, 217001 (2018).
- M. Fidyriak, M. Zegrodnik, J. Spalek, *Phys. Rev. B* **98**, 085436 (2018).
- L. Rademaker, P. Mellado, *Phys. Rev. B* **98**, 235158 (2018).
- D. M. Kennes, J. Lischner, C. Karrasch, *Phys. Rev. B* **98**, 241407 (R) (2018).
- Y.-Z. You, A. Vishwanath, arXiv:1805.06867 [cond-mat.str-el] (17 May 2018).
- J. González, T. Stauber, *Phys. Rev. Lett.* **122**, 026801 (2019).
- Y. Su, S.-Z. Lin, *Phys. Rev. B* **98**, 195101 (2018).
- Y. Sherkunov, J. J. Betouras, *Phys. Rev. B* **98**, 205151 (2018).
- J. F. Dodaro, S. A. Kivelson, Y. Schattner, X.-Q. Sun, C. Wang, *Phys. Rev. B* **98**, 075154 (2018).
- T. J. Peltonen, R. Ojajarvi, T. T. Heikkilä, *Phys. Rev. B* **98**, 220504(R) (2018).
- F. Wu, A. H. MacDonald, I. Martin, *Phys. Rev. Lett.* **121**, 257001 (2018).
- B. Lian, Z. Wang, B. A. Bernevig, arXiv:1807.04382 [cond-mat.mes-hall] (12 July 2018).
- E. Laksono et al., *Solid State Commun.* **282**, 38–44 (2018).
- M. Yankowitz et al., Replication Data for: Tuning superconductivity in twisted bilayer graphene, Version 1.0, Harvard Dataverse (2019); <https://doi.org/10.7910/DVN/FIMUEY>.

## ACKNOWLEDGMENTS

We thank J. Zhu and H. Zhou for experimental assistance and D. Shahar, A. Millis, O. Vafek, M. Zaletel, L. Balents, C. Xu, A. Bernevig, L. Fu, M. Koshino, and P. Moon for helpful discussions. **Funding:** Work at both Columbia and UCSB was funded by the Army Research Office under W911NF-17-1-0323. Sample device design and fabrication were partially supported by DOE Pro-QM EFRC (DE-SC0019443), A.F.Y. and C.R.D. separately acknowledge the support of the David and Lucile Packard Foundation. A portion of this work was performed at the National High Magnetic Field Laboratory, which is supported by National Science Foundation Cooperative Agreement no. DMR-1644779 and the state of Florida. K.W. and T.T. acknowledge support from the Elemental Strategy Initiative conducted by the MEXT, Japan, and the CREST (JPMJCR15F3), JST. **Author contributions:** M.Y., S.C., H.P., and Y.Z. fabricated the devices. M.Y., S.C., and H.P. performed the measurements and analyzed the data. D.G. loaded the pressure cell. K.W. and T.T. grew the BN crystals. A.F.Y. and C.R.D. advised on the experiments. The manuscript was written with input from all authors. **Competing interests:** The authors declare no competing interests. **Data and materials availability:** The data from this study are available at the Harvard Dataverse (45).

## SUPPLEMENTARY MATERIALS

[www.sciencemag.org/content/363/6431/1059/suppl/DC1](http://www.sciencemag.org/content/363/6431/1059/suppl/DC1)  
Materials and Methods  
Supplementary Text  
Figs. S1 to S11  
Table S1  
References (46–62)

24 August 2018; accepted 15 January 2019  
Published online 24 January 2019  
10.1126/science.aav1910

## Tuning superconductivity in twisted bilayer graphene

Matthew Yankowitz, Shaowen Chen, Hryhorii Polshyn, Yuxuan Zhang, K. Watanabe, T. Taniguchi, David Graf, Andrea F. Young and Cory R. Dean

*Science* **363** (6431), 1059-1064.

DOI: 10.1126/science.aav1910originally published online January 24, 2019

### Upping the pressure in bilayer graphene

The discovery of superconductivity and exotic insulating phases in twisted bilayer graphene has established this material as a model system of strongly correlated electrons. To achieve superconductivity, the two layers of graphene need to be at a very precise angle with respect to each other. Yankowitz *et al.* now show that another experimental knob, hydrostatic pressure, can be used to tune the phase diagram of twisted bilayer graphene (see the Perspective by Feldman). Applying pressure increased the coupling between the layers, which shifted the superconducting transition to higher angles and somewhat higher temperatures.

*Science*, this issue p. 1059; see also p. 1035

#### ARTICLE TOOLS

<http://science.sciencemag.org/content/363/6431/1059>

#### SUPPLEMENTARY MATERIALS

<http://science.sciencemag.org/content/suppl/2019/01/23/science.aav1910.DC1>

#### RELATED CONTENT

<http://science.sciencemag.org/content/sci/363/6431/1035.full>

#### REFERENCES

This article cites 54 articles, 5 of which you can access for free  
<http://science.sciencemag.org/content/363/6431/1059#BIBL>

#### PERMISSIONS

<http://www.sciencemag.org/help/reprints-and-permissions>

Use of this article is subject to the [Terms of Service](#)